# The *SLAM* Project: I. Description of Simulations

Marios Chatzikos

*Department of Physics & Astronomy, University of Kentucky, Lexington, KY 40506-0055*

mnc3z@astro.virginia.edu

and

Craig L. Sarazin

*Department of Astronomy, University of Virginia, P.O. Box 400325, Charlottesville, VA 22904-4325*

and

Brian W. O'Shea

*Department of Physics and Astronomy and Lyman Briggs College, Michigan State University, East Lansing, MI*

## ABSTRACT

This is the first in a series of papers describing astrophysical and cosmological results based on the *S*imulation *L*ibrary of *A*strophysical galaxy cluster *M*ergers (*SLAM*) database, consisting of a set of 156 adiabatic simulations of binary galaxy cluster mergers. The simulations were conducted with the TreeSPH code Gadget-2. In this paper, we describe the setup for these numerical experiments and demonstrate their convergence.

The present simulation set spans an unprecedented parameter space volume covering a factor of 200 in the mass of the primary cluster, one order of magnitude in the mass ratio of the merging components and 4 values for the orbital angular momentum of the merger. The models we use for the clusters prior to the collisions employ varying gas fractions and entropy profiles in agreement with recent *Chandra* findings. The initial cluster structures are in very good ($\sim 20\%$) agreement with detailed *Chandra* observations of galaxy clusters, and reproduce quite faithfully all of the observed scaling relations we have inspected. We resolve the primary cluster with one million particles, split in equal parts between the dark matter and the intracluster medium, while the subcluster is scaled according to its relative mass and gas fraction.

We demonstrate the convergence of our runs by exploring the properties of a resimulation of a high mass ratio, maximum offset collision which uses about an order of magnitude more particles. We compare the temporal variation of a set of cluster properties between the two runs and conclude that our simulations have converged for the adopted resolution.

*Subject headings:* galaxies: clusters: general — galaxies: groups: general — hydrodynamics — methods: numerical — X-rays: galaxies: clusters

## 1. Introduction

Clusters of galaxies are the most massive virialized structures in the Universe. Typically located at nodes in the cosmic web, clusters grow in mass via continuous accretion of infalling matter and violent collisions with other clusters called mergers.

Mergers are the most energetic in the Universe since the Big Bang, involving energies of up to $10^{64}$ erg. During a merger, the hot gas of the two clusters experiences hydrodynamical shocks that raise its temperature and entropy, effectively converting potential energy to thermal energy of the intracluster medium (ICM). In addition, shocks accelerate particles to relativistic speeds, which are seen in several merging clusters as diffuse radio relics (Skillman et al. 2011). They are also thought to establish turbulent cascades in the ICM, which act to enhance the magnetic field and accelerate particles that shine in cluster-centered diffuse radio halos (Ferrari et al. 2008; Brunetti & Lazarian 2011).

The detailed physics of the ICM has been the subject of much debate. Our confidence in modeling the hot cluster gas is limited by our restricted knowledge of the microscopic properties of the plasma. These properties include the plasma viscosity and conductivity, which may play an important role in heating the plasma, and affecting the scale of turbulent cascades and other microscopic processes such as diffusion and mixing. These properties are important for the stability of cool cores and for averting the cooling catastrophe (Ruszkowski & Oh 2010). In principle, the study of realistic cluster mergers should involve an accurate description of the plasma properties, as well as modeling all relevant physical processes. However, this is not currently possible, as many of the mechanisms involved in cluster mergers are currently not well understood. On the other hand, the properties of cluster mergers have not been extensively investigated, as clusters have been thought of as scale-free systems. Recent *Chandra* and *XMM-Newton* observations have revealed differences between massive clusters and galaxy groups, which warrant a fresh look at collisions of galaxy clusters, an approach we follow in this work.

Idealized mergers have been used extensively in the past to study cluster collisions in much greater detail than typically afforded by cosmological simulations. Early work on this field investigated the propagation of shocks through the cluster atmosphere, their impact on the thermodynamics and equipartition of the ICM (e.g., Pearce et al. 1994; Takizawa 1999), as well as the geometry and longevity of transient complex structures in the gas density and temperature and their implications for X-ray observations (e.g., Roettiger et al. 1996, 1997). Other investigators (e.g., Ricker 1998; Ricker & Sarazin 2001; Ritchie & Thomas 2002) focused on the dynamics of the merging system and the evolution of X-ray observables, such as the X-ray luminosity and emission-weighted temperature, and concluded that these proxies undergo brief boosts by factors of $\sim$2–10 that could bias cosmological surveys (Randall et al. 2002; Wik et al. 2008). More recently, idealized collisions have been used to study the effects of mergers on the survival of cool cores (Poole et al. 2006, 2008), as well as the efficiency of mixing between the gaseous atmospheres of the two merging clusters (Mitchell et al. 2009; ZuHone 2011).

In this series of papers, we conduct an extensive parametric study of the effects of mergers on the dynamics of clusters, as well as on merging signatures in the X-rays and the microwave through the Sunyaev-Zel'dovich effect (SZE). The ultimate goal of this study is to understand the biases that mergers introduce in X-ray and SZE observations of galaxy clusters, and correlate them to the true dynamical state of the system. By extension, we aim to quantify the influence of cluster collisions on the output of cosmological surveys conducted in these bands. Although the most realistic approach to measuring effects on galaxy cluster populations would be to conduct cosmological simulations, we have opted to perform idealized experiments in which the parameters of interest can be controlled directly, and their influence can be explored more readily. This also enables us to study mergers in much greater spatial and temporal detail than a cosmological simulation would permit, particularly at the low-mass end of the cluster mass function. For instance, we follow the merger of two $10^{13}\,M_\odot$ clusters, each modeled with $10^6$ particles, which corresponds to a mass resolution of $10^7\,M_\odot$, or two orders of magnitude better than the dark matter (DM)-only *Millennium Simulation* (Springel et al. 2005), and about 3 orders of magnitude better than the *MareNostrum Numerical Cosmology Project* (Gottlöber & Yepes 2007).

Our experiments are idealized in several ways. Firstly, the binary mergers are assumed to occur in isolation from the rest of the Universe, such that each cluster operates only under the gravitational influence of its merging partner. That is, large scale tidal fields are not incorporated in these calculations. Furthermore, the initial structures of the colliding systems are typical of low-redshift relaxed clusters, which are characterized primarily by the presence of an entropy floor at the cluster center. In fact, as we will see below, we have developed a model for the initial cluster structure that is in very good agreement with *Chandra* and

*XMM-Newton* observations of relaxed clusters. Finally, the simulations are adiabatic, due to the fact that we are mainly interested in the cluster outskirts, while gas cooling is known to primarily affect the cluster core. Similarly, heating by means of supernovae, AGN outflows, galactic winds and star formation is presently ignored.

The set of simulations discussed herein consists of 156 runs, which we refer to as the *S*imulation *L*ibrary of *A*strophysical galaxy cluster *M*ergers (*SLAM*).

In this first paper, we describe the initial cluster models and the convergence of simulations. In §2 we present the theoretical model used with the generation of initial cluster structures, while in §3 we describe the particle realizations of the clusters and their initial dynamics. We discuss the method of choice for cluster detections in §4, and the convergence of calculations in §5. We summarize our results in §6. In this work, we adopt the *WMAP* 5-year results (Komatsu et al. 2009) as the reference cosmology.

## 2. Initial Cluster Structures

### 2.1. Approach

We describe a semi-analytical model of cluster structure based on empirical relations of relaxed and cool-core clusters and groups, derived mainly from *Chandra* and *XMM-Newton* observations. The model is constructed assuming spherical symmetry, hydrostatic equilibrium and convective stability. While its purpose is mainly to serve as the blueprint for initializing our merging clusters, we have tried to keep it as faithful to observations as possible.

Our initial model clusters form a continuous, one-parameter sequence in which the mass is the only important physical scale and self-gravity is the dominant force in determining the internal structure of the system.

However, our initial models are not self-similar. For such a distribution of the ICM, aggregate cluster observables are expected to follow scaling laws that are not supported by observations. For example, while the X-ray luminosity ($L_X$) and temperature ($T_X$) are expected to scale as $L_X \propto T_X^2$, observations reveal a steeper correlation, $L_X \propto T_X^3$ (e.g., Edge & Stewart 1991; Osmond & Ponman 2004; Pratt et al. 2009).

Several lines of evidence have emerged over the last few years that indicate that non-gravitational physical processes can also affect the dynamics of the ICM. For instance, the interplay of X-ray cooling, heating by AGN outflows, and at a lesser degree, star formation and supernovae, appear to have an important effect on the ICM at the centers of some galaxy

clusters. These processes act to introduce, redistribute, or remove thermal energy from the X-ray gas. Although currently unconstrained by observations, these processes leave their imprint on the entropy of the ICM, and cause it to deviate from the self-similar expectation.

*Chandra* and *XMM-Newton* have greatly improved our knowledge of the ICM entropy profiles. The emerging picture is that the entropy scales according to self-similarity at the cluster outskirts, while at the cores the state of the gas correlates with the dynamical state of the cluster at large (Pratt et al. 2010). This suggests that non-gravitational effects are dynamically relevant only at the cluster centers, while the gas in the outskirts is approximately adiabatic.

Our aim is to construct realistic models of relaxed cluster, which in principle require a detailed description of all relevant physical processes. As this is not currently feasible, we have opted to approximate the ICM with an adiabatic gas whose entropy distribution encapsulates the effects of non-thermal processes. The gas structure is solved for subject to the adopted entropy law and dark matter gravitational potential.

### 2.2. Model Details

We assume that all clusters are spherical, in hydrostatic equilibrium, and convectively stable.

We employ the usual definition for the mass of a cluster within a radius that encompasses a specific density contrast ($\Delta$) with respect to the critical density at redshift, $z$. The enclosed mass is related to the radius via

$$M_\Delta = \frac{4\pi}{3}\, R_\Delta^3\, \Delta\rho_c(z=0)\,. \tag{1}$$

We take the redshift to be $z = 0$ for convenience, because the model is calibrated against low-redshift clusters; the particular choice does not affect our results significantly. We adopt the usual definition ($\Delta = 200$; e.g., Kaiser 1986) for the virial mass of the cluster.

Most of the cluster mass is in the form of dark matter. Note that we ignore the stellar content (galaxies and intracluster light) of clusters, and treat it as part of the collisionless component. We assume that the dark matter mass is distributed according to the NFW density profile (Navarro et al. 1997),

$$\rho_{\rm DM}(r) = \rho_s (r/r_s)^{-1}(1 + r/r_s)^{-2}\,, \tag{2}$$

where $\rho_s$ and $r_s$ are the characteristic density and the scale radius, respectively. The concentration parameter of the dark matter halo is defined as $c = R_{200}/r_s$. Equation (2) is fully

determined by employing the observed X-ray concentration-mass relation of Buote et al. (2007) to set the scale radius. Note that their $c$–$M$ relation refers to an overdensity of 100 relative to the critical density; we convert to our fiducial overdensity of 200 by following the procedure of Hu & Kravtsov (2003).

The only other constituent in our model is the X-ray gas. In agreement with observations, we adopt for the gas mass fraction, $f_{\rm gas}$, a form that depends on the system mass, that is,

$$f_{\rm gas}(M_{200}) = 0.115\, h_{70}^{-1.5} \left(\frac{M_{200}}{10^{14} h_{70}^{-1} M_\odot}\right)^{0.094}, \tag{3}$$

where $h_{70}$ is the present value of the Hubble constant in units of 70 km s$^{-1}$ Mpc$^{-1}$. This form offers a good approximation to the observed gas fractions over the entire mass range covered by galaxy clusters. The quality of its agreement to the relations of Vikhlinin et al. (2009) and Sun et al. (2009, hereafter S09) is presented in Figure 1.

We derive the gas structure by employing a parametric form for the entropy profile. In practice, the X-ray entropy accessible to observations is defined as

$$K_e = \frac{kT_e}{n_e^{2/3}}\,, \tag{4}$$

where $T_e$ and $n_e$ are the electron temperature and density, respectively. The connection to the gas entropy is established by assuming that the various particle populations have reached equipartition at a common temperature, so that

$$K = \frac{P_{\rm gas}}{\rho_{\rm gas}^{5/3}} = \frac{(n_e/n)^{2/3}}{(\mu m_p)^{5/3}}\, K_e\,, \tag{5}$$

where $n$ is the total gas density, $\mu$ is the plasma mean molecular weight, and $m_p$ the proton mass. We adopt a flat abundance profile for our clusters at 30 percent of the cosmic abundances of Anders & Grevesse (1989); for this abundance, $\mu = 0.61$ and $n_e/n = 0.52$.

We adopt an increasing, offset power-law distribution for the entropy profile, in agreement with the observed entropy profiles of relaxed clusters and groups, which guarantees convective stability throughout the cluster volume,

$$K_e(r) = K_0 + K_{0.1\,{\rm R}_{200}} \Big(\frac{r}{0.1 R_{200}}\Big)^{\alpha}; \tag{6}$$

here, the central entropy floor and the power-law index vary linearly with $\log M_{200}$. We determine the linear ramp for the central entropy by requiring that a $10^{15}\,M_\odot$ cluster have a core entropy of 10 keV cm$^2$, in accordance with Donahue et al. (2006), and that a $10^{13}\,M_\odot$ cluster have a central entropy of 2 keV cm$^2$. The power-law indices are determined by a

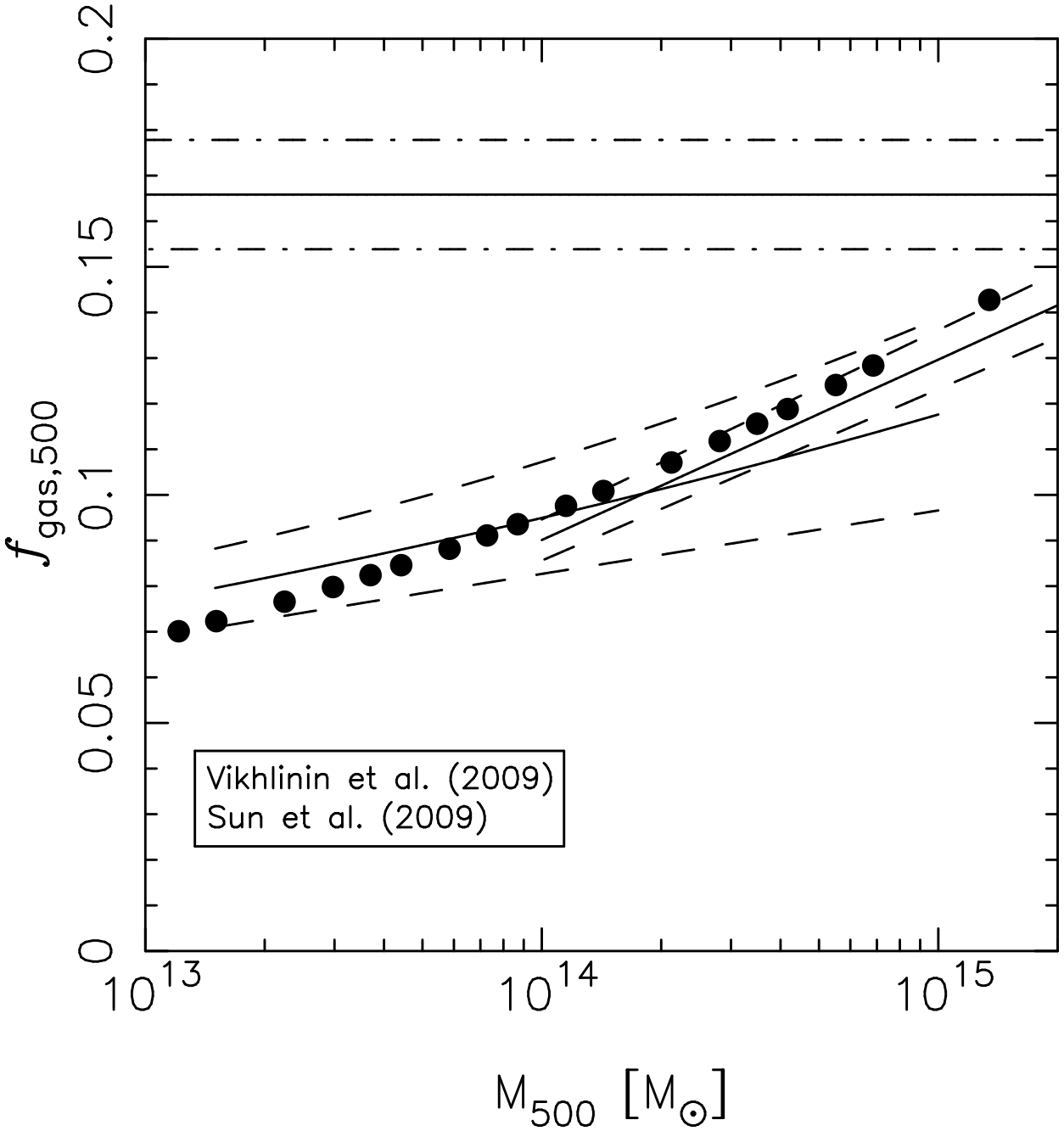


Fig. 1.— Comparison of the gas fractions within $R_{500}$ of the initial structures used in our simulations with the $f_{\rm gas}(M)$ relations of Vikhlinin et al. (2009) (red lines) and S09 (green lines), observed with *Chandra*. The dashed lines include the uncertainties in the fits. All curves have been adjusted to our preferred cosmology. Note that the Vikhlinin et al. (2009) relation (colored red in the online version) is valid in the range (1–20)$\times10^{14}\,M_\odot$, while the S09 relation (colored green) is valid in the range (0.15–10)$\times10^{14}\,M_\odot$. The horizontal solid and dash-dotted lines represent the cosmic gas fraction and its error, respectively, for the cosmology of choice.

parameter space search as described below. We adopt the "entropy ramp" of Ponman et al. (2003) and Piffaretti et al. (2005) for the normalization of the entropy profile; that is, we allow the entropy at $0.1R_{200}$ to scale as

$$K_{0.1\,\mathrm{R}_{200}} = K_{\mathrm{const}}\,(T/10\,\mathrm{keV})^{0.65}\,. \tag{7}$$

The normalization, $K_{\mathrm{const}}$, is also determined empirically. An initial estimate for the temperature is required for using this formalism, which we obtain by employing the observed $M-T$ relation of Sanderson et al. (2003).

We use the entropy profile in place of the pressure in the hydrostatic equation and arrive at the system of differential equations:

$$\frac{dM_{\mathrm{gas}}}{dr} = 4\pi r^2 \rho \tag{8}$$

$$\frac{d\rho}{dr} = -\frac{3}{5K(r)}\left\{\frac{dK(r)}{dr}\rho + \frac{G[M_{\mathrm{DM}}(<r)+M_{\mathrm{gas}}(<r)]}{r^2}\rho^{5/3}\right\}, \tag{9}$$

which is constrained given the boundary values for the gas and DM mass within $R_{200}$.

### 2.3. Calibration and Comparison to Observations

As mentioned above, the parameters for the entropy profiles are determined by optimizing our models against the data of Vikhlinin et al. (2006, hereafter V06a). We used 12 of the 13 clusters presented in that work, with the exception of USGC S152 for which $R_{500}$ is not constrained. For each object, we adjust the total mass and solve for the cluster structure until the mass within $R_{500}$ agrees with the measured mass to better than 1 part in $10^5$. We also compare the properties of the sample as a whole against known scaling relations of cool core and relaxed clusters.

We have computed ∼5,100 distinct models that cover an extensive volume of parameter space for the free parameters, and we have determined that very satisfactory results are produced by the combination ($K_{\mathrm{const}}$, $\alpha_{13}$, $\alpha_{15}$) = (450 keV cm$^2$, 0.4, 0.9). Here, $\alpha_{13}$ and $\alpha_{15}$ are the power-law indices of the entropy profile of $10^{13}\,M_\odot$ and $10^{15}\,M_\odot$ clusters, respectively, used with the linear ramp of entropy index for our cluster models. Note that, another set of satisfactory results may be obtained by a lower normalization ($K_{\mathrm{const}} = 350\,\mathrm{keV\,cm^2}$), but we ignore it as it contradicts other observations.

For these optimal values, the comparison of our instances of the V06a models to the observations is generally favorable. Our procedure does not reproduce the density profiles

of these clusters faithfully (Fig. 2, left panel); the reconstructed clusters are underdense by 20–30% within $\sim 0.6 \times R_{500}$, but recover to the observed values by about $R_{500}$. Despite the deviations, the temperature profiles are within 20% of the observed, and the discrepancies are even smaller if the profiles are normalized by the gas-mass-weighted temperature (Fig. 2, right panel), particularly for hot clusters. This behavior is consistent with the 15% of variance in the temperature profiles measured by V06a, and reflects the fact that our models produce faithful descriptions of the cluster structure.

The reconstructed V06a models are also in very good agreement with various observed and simulated scaling relations. Figure 3 presents a subset of the scaling relations to which we compared these clusters. The observed best-fit relations are shown along with their errors and intrinsic scatter (where available), and our results are in excellent agreement with them. Although one would expect the cluster properties on the $L_X$–$Y_X$ plane, where $L_X$ is the X-ray luminosity and $Y_X$ is the X-ray equivalent of the integrated SZE decrement, to be affected by the discrepancies in the density profiles, this is not observed due to the fact that the model profiles deviate from the true ones mostly near the center, while beyond $0.15R_{500}$ the majority of models are well within 30% of the V06a fits. The overall effect is to shift the clusters on the $L_X$–$Y_X$ plane parallel to the observed relation. Likewise, in the $M_{500}$–$Y_X$ plane the observed clusters are shifted toward lower temperatures only by small amounts. Note that for the calculation of $Y_X$ in these relations, we employed the spectral projection method of Vikhlinin (2006) for a *Chandra ACIS* calibration produced with the mixT[1] code. We also employed the same energy bands for the $T_X$ calculations as used in the derivation of the scaling relations, although this does not affect the scaling of the models significantly.

The empirically determined parameter set ($K_{\rm const}$, $\alpha_{13}$, $\alpha_{15}$) = (450 keV cm$^2$, 0.4, 0.9) is in reasonable agreement with a variety of observations. The normalization constant is consistent with observations of nearby cool core clusters. For instance, Piffaretti et al. (2005) find an entropy scale at 10 keV of $504 \pm 140$ keV cm$^2$, while Morandi & Ettori (2007) report an entropy normalization of $509 \pm 130$ keV cm$^2$ for the strong cool core clusters in their sample ($T_{ew} > 7$ keV).

The average power-law index of our modeled groups (systems with core-excised temperatures $T_{500} < 2.7$ keV) is $0.57 \pm 0.10$, in agreement with the results of S09 (Figure 14 therein), and Finoguenov et al. (2007), who find slopes in the range 0.6–0.75. On the other hand, the mean entropy slope of massive clusters, $T_{500} > 2.7$ keV, is $0.85 \pm 0.06$. For the subsample of our clusters that best matches the work of Piffaretti et al. (2005), 1.2 keV $< T_{500} <$ 6.8 keV, the average entropy slope is $0.77 \pm 0.09$, which constitutes a 2-$\sigma$ deviation from the reported

[1]http://hea-www.harvard.edu/~alexey/mixT/

$0.95 \pm 0.02$. However, this difference arises because we model clusters and groups in a unified fashion. Indeed, by adopting a constant power-law index, $\alpha_{15} = \alpha_{13} = 0.95$, the agreement with the $M$–$T_{\rm mg}$ relation (V06a) does not extend below 4.5 keV. In addition, this constant power-law index leads to entropy profiles for galaxy groups that disagree with the observations of S09. This suggests that in principle a mass-dependent power-law index may be preferable. However, although for massive clusters the power-law index is not consistent with observations, their aggregate properties are not particularly sensitive to the exact value.

Overall, although the optimal parameter values are on the shallow end of the observed range, they reproduce the observed clusters and groups quite faithfully. For completeness, we have explored a set of higher values that are in better agreement with the observations, that is, $(K_{\rm const}, \alpha_{13}, \alpha_{15}) = (500\,{\rm keV\,cm^2}, 0.6, 1.1)$, but the produced clusters are hotter than the observed clusters by about 30% at all scales on the $M_{500}$–$T_{\rm mg}$ plane.

A more detailed examination of the entropy properties of our models, offered in Appendix A, demonstrates that for the optimal entropy scaling the profiles at various radii from the cluster center are in excellent agreement with the findings of S09 within $R_{1000}$, with 1–2-$\sigma$ discrepancies occurring near $R_{500}$ for cooler systems. The scaling properties for all initial models is presented in Appendix B.

Our analysis indicates that despite any remaining discrepancies, our models offer a very satisfactory description of observed clusters and groups. In the following, we use these models to set up the initial conditions of our simulations for collisions of clusters in the mass range $10^{13}$–$2\times10^{15}\,M_\odot$. The structural parameters of the initial clusters are presented in Table 1 along with some key observational properties.

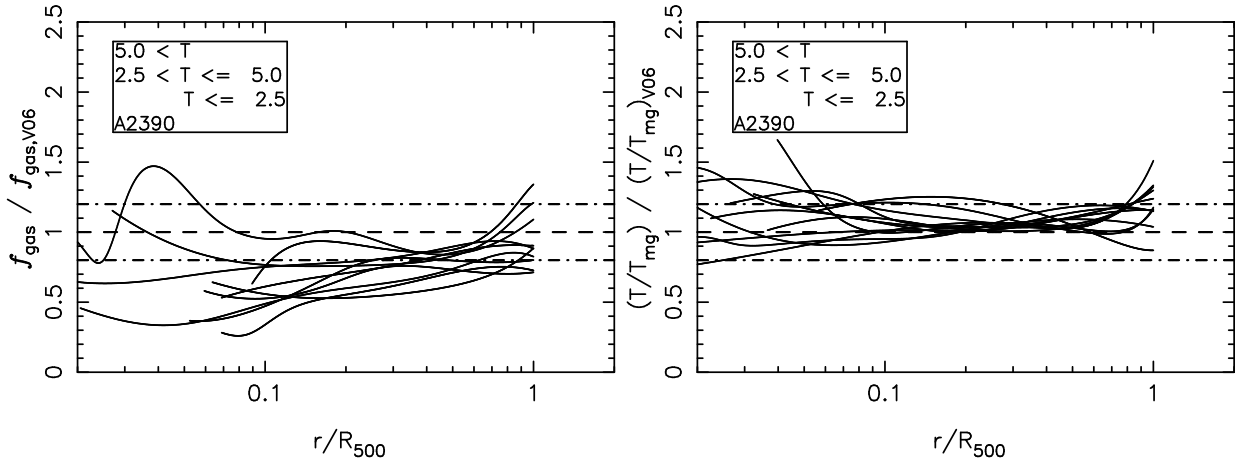


Fig. 2.— Comparison of the radial gas distribution of our reproductions of the Vikhlinin et al. (2006) clusters against the observations. We adopt the same color scheme as in that paper; note that AGN bubbles are present near the center of Abell 2390. *(Left)* Gas fraction profiles within $R_{500}$ for those V06a systems with measured $f_{\rm gas}$. *(Right)* Temperature profiles scaled by the mass weighted temperature. Our models are successful at reproducing the observed temperature distribution, but are somewhat underdense near the center (see text).

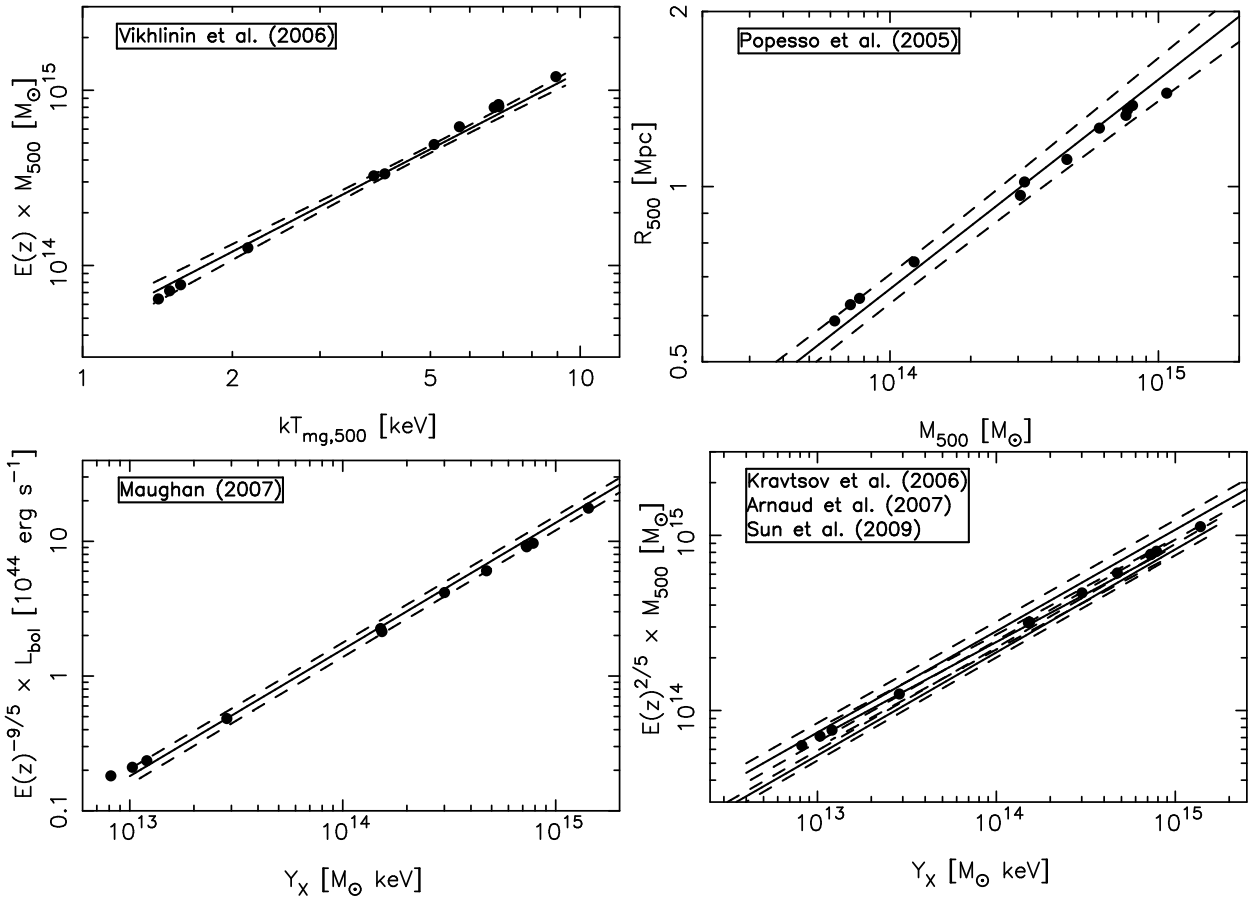


Fig. 3.— Comparison of the properties of our fiducial V06a models against observed scaling relations. Note that the dashed lines incorporate the errors and intrinsic scatter (if measured) in the best-fit relations. *(Top, Left)* $M_{500}$–$T_{\rm mg}$ relation obtained by Vikhlinin et al. (2006). *(Top, Right)* $R_{500}$–$M_{500}$ relation from SDSS clusters of Popesso et al. (2005). *(Bottom, Left)* $L_{\rm bol}$–$Y_X$ relations obtained by Maughan (2007). *(Bottom, Right)* $M_{500}$–$Y_X$ relation obtained from observations by Arnaud et al. (2007) and S09, and from simulations by Kravtsov et al. (2006), corrected for the lower cosmic gas fraction adopted therein.

Table 1. Initial Cluster Properties

| $M_{200}$ ($10^{13}\,M_\odot$) (1) | $M_{500}$ ($10^{13}\,M_\odot$) (2) | $c_{200}$ (3) | $R_{200}$ (Mpc) (4) | $R_{500}$ (Mpc) (5) | $f_{\rm gas,500}$ (Mpc) (6) | $L_X$[a] ($10^{43}$ erg s$^{-1}$) (7) | $T_X$[b] (keV) (8) | $L_{\rm X,exc}$[c] ($10^{43}$ erg s$^{-1}$) (9) | $T_{\rm X,exc}$[d] (keV) (10) | $Y_X$[e] ($10^{13}\,M_\odot$ keV) (11) |
|---|---|---|---|---|---|---|---|---|---|---|
| 200 | 134.507 | 3.781 | 2.596 | 1.676 | 0.142 | 256.917 | 9.588 | 139.834 | 9.89 | 179.985 |
| 100 | 68.524 | 4.293 | 2.061 | 1.338 | 0.128 | 88.771 | 6.368 | 51.333 | 6.62 | 54.537 |
| 80 | 55.15 | 4.471 | 1.913 | 1.245 | 0.124 | 62.555 | 5.585 | 36.759 | 5.806 | 37.231 |
| 60 | 41.683 | 4.712 | 1.738 | 1.134 | 0.118 | 39.603 | 4.704 | 23.709 | 4.905 | 22.664 |
| 50 | 34.905 | 4.871 | 1.635 | 1.069 | 0.115 | 29.529 | 4.226 | 17.867 | 4.412 | 16.568 |
| 40 | 28.089 | 5.073 | 1.518 | 0.994 | 0.111 | 20.542 | 3.689 | 12.579 | 3.864 | 11.26 |
| 30 | 21.226 | 5.345 | 1.379 | 0.905 | 0.107 | 12.1 | 3.096 | 7.511 | 3.262 | 6.824 |
| 20 | 14.299 | 5.752 | 1.205 | 0.794 | 0.1 | 6.564 | 2.391 | 4.144 | 2.542 | 3.333 |
| 16 | 11.504 | 5.989 | 1.118 | 0.738 | 0.097 | 4.543 | 2.058 | 2.9 | 2.203 | 2.22 |
| 12 | 8.69 | 6.309 | 1.016 | 0.672 | 0.093 | 2.862 | 1.681 | 1.849 | 1.797 | 1.322 |
| 10 | 7.274 | 6.52 | 0.956 | 0.633 | 0.091 | 2.156 | 1.467 | 1.405 | 1.603 | 0.947 |
| 8 | 5.85 | 6.788 | 0.888 | 0.589 | 0.088 | 1.546 | 1.31 | 1.021 | 1.388 | 0.655 |
| 6 | 4.418 | 7.148 | 0.806 | 0.536 | 0.084 | 1.033 | 1.096 | 0.697 | 1.168 | 0.4 |
| 5 | 3.697 | 7.387 | 0.759 | 0.505 | 0.082 | 0.812 | 1.005 | 0.555 | 1.066 | 0.296 |
| 4 | 2.973 | 7.689 | 0.704 | 0.47 | 0.079 | 0.611 | 0.885 | 0.425 | 0.94 | 0.204 |
| 3 | 2.244 | 8.096 | 0.64 | 0.428 | 0.076 | 0.397 | 0.77 | 0.282 | 0.814 | 0.128 |
| 2 | 1.509 | 8.706 | 0.559 | 0.375 | 0.072 | 0.249 | 0.623 | 0.179 | 0.657 | 0.065 |
| 1.6 | 1.213 | 9.06 | 0.519 | 0.348 | 0.07 | 0.182 | 0.548 | 0.131 | 0.583 | 0.044 |
| 1.2 | 0.915 | 9.538 | 0.471 | 0.317 | 0.067 | 0.117 | 0.452 | 0.084 | 0.486 | 0.026 |
| 1 | 0.765 | 9.853 | 0.444 | 0.299 | 0.065 | 0.087 | 0.401 | 0.062 | 0.43 | 0.019 |

[a]Total luminosity computed in the energy range 0.6–10 keV.

[b]Total spectroscopic temperature according to V06a, computed in the same range as $L_X$, and with a column density of $4 \times 10^{20}$ cm$^{-2}$.

[c]Core-excised luminosity computed in the same energy range as $L_X$, but in the projected radial range $(0.15–1)\times R_{500}$.

[d]Spectroscopic temperature according to V06a, computed in the same range as $L_{\rm X,exc}$, and with a column density of $4 \times 10^{20}$ cm$^{-2}$.

[e]Computed using $\rm T_{X,exc}$.

## 3. Initial Conditions

### 3.1. Initial Cluster Models and Realizations

The models described above require further processing before they are used in the initial conditions of the simulations. The calculations extend out to $R_{200}$ but an additional envelope is required to preserve their initial structures until the collision begins. We have employed additional solutions for both the DM and the ICM that extend beyond $R_{200}$, in a fashion similar to Kazantzidis et al. (2004) and Poole et al. (2006).

For the dark matter, we use a density profile similar to the one adopted by Kazantzidis et al. (2004):

$$\rho_{\rm DM}(r) = \frac{\rho_s}{c(1+c)^2}\left(\frac{r}{R_{200}}\right)^{\epsilon}\exp\left(-\frac{r-R_{200}}{R_{\rm decay}}\right) \qquad R_{200} \leq r\,, \tag{10}$$

where the first term on the right-hand side is the density at $R_{200}$, $R_{\rm decay}$ is a suitable parameter that controls the extent of the envelope and $\epsilon$ is set by the requirement that the density derivative be continuous across the virial radius. In our calculations we have taken $R_{\rm decay}/R_{200} = 0.265$.

We have extended the hydrostatic solution of the gas halo out to $R_{100}$, roughly 4/3 of $R_{200}$, to guarantee stability across the virial radius. In fact, this is the reason behind using a somewhat large value for the dark matter decay radius, as we wish the envelope mass to be dominated by dark matter out to $R_{100}$. Beyond that, we have employed a steeper exponential envelope of the form:

$$\frac{\rho_{\rm ICM}(r)}{\rho_{\rm ICM}(R_{100})} = \left(\frac{r}{R_{100}}\right)^{\epsilon_{\rm ICM}}\exp\left[-\left(\frac{r-R_{100}}{R_{\rm decay,ICM}}\right)^{\nu}\right]\,. \tag{11}$$

The envelope is extended until the pressure drops to a common value for all clusters, typical for the intergalactic medium (IGM). In practice, we follow Poole et al. (2006) and set the outer pressure to $P_{\rm IGM} = (\Omega_B\rho_c/\mu m_p)kT_{\rm IGM} \approx 2\times10^{-17}$ erg cm$^{-3}$, where $\Omega_B$ is the baryon density parameter in the Universe today, and $T_{IGM} = 3\times10^5$ K is our adopted intergalactic medium temperature. We have found that the choice of $R_{\rm decay,ICM} = 3R_{\rm decay}$ and $\nu = 2$ produces the most stable halos for the smallest overhead. The final halos have outer radii of $\sim 2.15$–$2.35 \times R_{200}$, while their total masses are inflated by $\sim$35% compared to $M_{200}$. In our realizations of the initial conditions, discussed below, we employ an IGM-like external medium to confine the clusters gas.

The last ingredient required for our recipe is the dark matter velocity field. Typically researchers employ a Maxwellian distribution, obtained as the solution to the Jeans equation

for the system at hand. However, Kazantzidis et al. (2004) showed that when this procedure is applied to halos that possess a central density cusp, such as those used in this work, the cusp is erased after just one crossing time. Instead, they found that halos initialized by employing a numerical solution for the phase-space distribution function (DF) are robust for several crossing times. We follow the recommendations of Kazantzidis et al. (2004) and set the initial velocity field of our halos according to the DF method. We assume that the velocity dispersion of the dark matter particles is isotropic. According to the Jeans theorem, spherical systems with isotropic dispersions stem from DFs that depend only on the particle energy (see Binney & Tremaine 1987):

$$f(\mathcal{E}) = \frac{1}{\sqrt{8}\pi^2}\left[\int_0^{\mathcal{E}} \frac{d^2\rho_{\rm DM}}{d\Psi^2}\frac{d\Psi}{\sqrt{\mathcal{E}-\Psi}} + \frac{1}{\sqrt{\mathcal{E}}}\left(\frac{d\rho_{\rm DM}}{d\Psi}\right)_{\Psi=0}\right]. \tag{12}$$

In this equation, $\Psi = -\Phi$ is the relative potential (binding energy) and $\mathcal{E} = \Psi - \frac{1}{2}v^2$ is the relative energy. The derivative in the last term is estimated at infinity and vanishes for our model. We obtain the potential as the sum of two components. The dark matter potential is computed with an analytical integration of the Poisson equation, while the ICM potential via numerical integration. We rewrite the term $d^2\rho_{\rm DM}/d\Psi^2$ in terms of first and second order radial derivatives for the density and the potential, and tabulate the results; during integration, we employ a polynomial interpolation scheme to generate values for the integrand. We have made certain that $f(\mathcal{E}) \geq 0$ for all halos and we have verified that the integral

$$\int_0^{\mathcal{E}} \frac{d\rho_{\rm DM}}{d\Psi}\frac{d\Psi}{\sqrt{\mathcal{E}-\Psi}} \tag{13}$$

is monotonically increasing throughout the cluster volume. We have finally confirmed that the dark matter density profile computed from the DF as

$$\rho_{\rm DM}(r) = \int_0^{\sqrt{2\Psi(r)}} f[\Psi(r) - \frac{1}{2}v^2]\; v^2 dv \tag{14}$$

is in good agreement with the exact profile throughout the cluster virial region.

As we discuss in more detail below, we use Gadget-2 (Springel 2005) for our simulations. We model each primary halo with 1,000,000 particles, equally split between the dark matter and gas, and scale the particle numbers of the subcluster according to the mass and gas fraction ratios of the two clusters. We initialize the particles in our halos using the acceptance-rejection technique (Press et al. 1992). For each particle, we draw a uniform deviate in the range [0,1] for the fraction of cumulative mass enclosed within the particle's radius, and invert the appropriate mass profile to obtain the distance to the cluster center. We determine the other spherical coordinates (polar and azimuthal angles) by drawing two

additional random numbers. For gas particles, this automatically sets the temperature as well. (The density is evaluated from the particle distribution by the simulation code.) For a dark matter particle, we also need to set the velocity vector. We employ the acceptance-rejection method as follows (see also Kuijken & Dubinski 1994). From the value of the potential at the given radius we evaluate the maximum velocity a particle may have, and use the product $v_{\rm max}^2 f(v_{\rm max})$ as the comparison function for the purposes of the rejection algorithm. We take the integrand of equation (14) as the probability function we wish to reproduce. We draw uniform deviates to compute the integrand $v^2 f(v, \Psi)$, and to randomly sample the comparison function. If the sampled value is less than the value of the integrand, we accept the velocity; otherwise, we repeat this process.

As mentioned above, we embed our clusters in a confining medium whose density and temperature are characteristic of the intergalactic medium. In order to limit the associated overhead, we place the particles in shells of progressively higher particle masses, starting with the mass value used within the clusters and increasing by factors of 10. About 50,000–70,000 additional particles are required to model the external medium, of which about 700–1400 are in massive particles at the outskirts of the computational volume. We have assigned these particles to circular polar orbits about the center of mass of the system and we have confirmed that at no time in any simulation do they penetrate the cluster volumes.

We have tested the stability of this procedure by placing clusters of various masses at the center of the computational volume and allowing them to evolve for about two billion years, the typical time interval between the start of our simulations and the beginning of the collision. In these test simulations, we witnessed little evolution in the cluster structure within the virial region, for both the gas and the dark matter properties of our halos. However, our sampling is too coarse to allow adequate modeling of the cluster centers.

### 3.2. Parameter Space Coverage

The problem of idealized binary mergers involves three free parameters: the mass of the primary cluster, $M_P$, the mass of the subcluster, $M_S$, and the dimensionless spin parameter of the collision, $\lambda$. In this work, we improve on previous studies of binary collisions by exploring the merging properties of massive clusters as well as groups in a uniform fashion. We thus cover a wide range of values for the mass of the primary cluster, namely (1–200)$\times 10^{13}\,M_\odot$, with a dense sampling of 12 distinct masses: 1, 2, 4, 6, 8, 10, 20, 40, 60, 80, 100 and 200. (In this work, unless otherwise specified, cluster masses are always in units of $10^{13}\,M_\odot$.)

In cosmological simulations it is customary to adopt an upper limit for the mass ratio

of merging systems, $M_P/M_S$, in order to distinguish "mergers" from "steady accretion". A typical value for that ratio is ∼10 (e.g., Faltenbacher et al. 2005), with higher values signifying more quiescent accretion events. In the present work, we have adopted this cutoff and we have chosen to investigate collisions of systems with mass ratios in the range 1 to 10, using 4 distinct values for $M_P/M_S = 1$, 2, 5 and 10. Note that in producing merging pairs we employ a lower mass limit of $10^{13}\,M_\odot$ for the mass of the subcluster.

Finally, we need a method for selecting values for the spin parameter of the collision, i.e., the orbital angular momentum. Numerical experiments (Bullock et al. 2001; Vitvitska et al. 2002) demonstrate that the spin parameter follows a universal log-normal distribution with a median value $\sim 0.044$ and a (log-normal) dispersion $\sim 0.5$, independent of halo mass and redshift. We use 4 values to sample the observed range of angular momenta, i.e., $\lambda = 0$, 0.025, 0.05, and 0.075. We study the case $\lambda = 0$ (head-on mergers) as it provides an upper limit to the possible effects of mergers on X-ray and SZE observables, despite the fact that it is not warranted from the numerical work mentioned above. On the other hand, Vitvitska et al. (2002) have shown that mergers with $\lambda = 0.1$ are somewhat likely to occur; yet, we do not simulate such high $\lambda$ values for practical reasons and because their effects can in principle be extrapolated from the other cases.

All in all, we have produced 156 simulations for the 39 mass ratios obtained for our choice of parameters.

### 3.3. Initial Kinematics

The simulations possess a simple geometry, similar to the one employed by Ricker & Sarazin (2001, RS01), shown for clarity in Figure 4. We set the clusters in contact at a distance equal to the sum of their $R_{100}$ radii, and determine their kinematics self-consistently based on the simple model of Sarazin (2002). To determine the initial velocity, we approximate the clusters as point-masses and assume that they broke off the Hubble expansion, and started falling back onto each other at the turnaround radius

$$d_0 = \left[2G\left(M_P + M_S\right)\right]^{1/3} \left(\frac{t_m}{\pi}\right)^{2/3} , \tag{15}$$

and that they merge at $t_m$, which we take to be the age of the Universe at the time of the merger; the exact value of $t_m$ does not affect our results significantly. The clusters then follow Keplerian orbits determined by their mutual gravity and the angular momentum at the turnaround radius.

We improve upon the model of Sarazin (2002) by computing self-consistent Keplerian

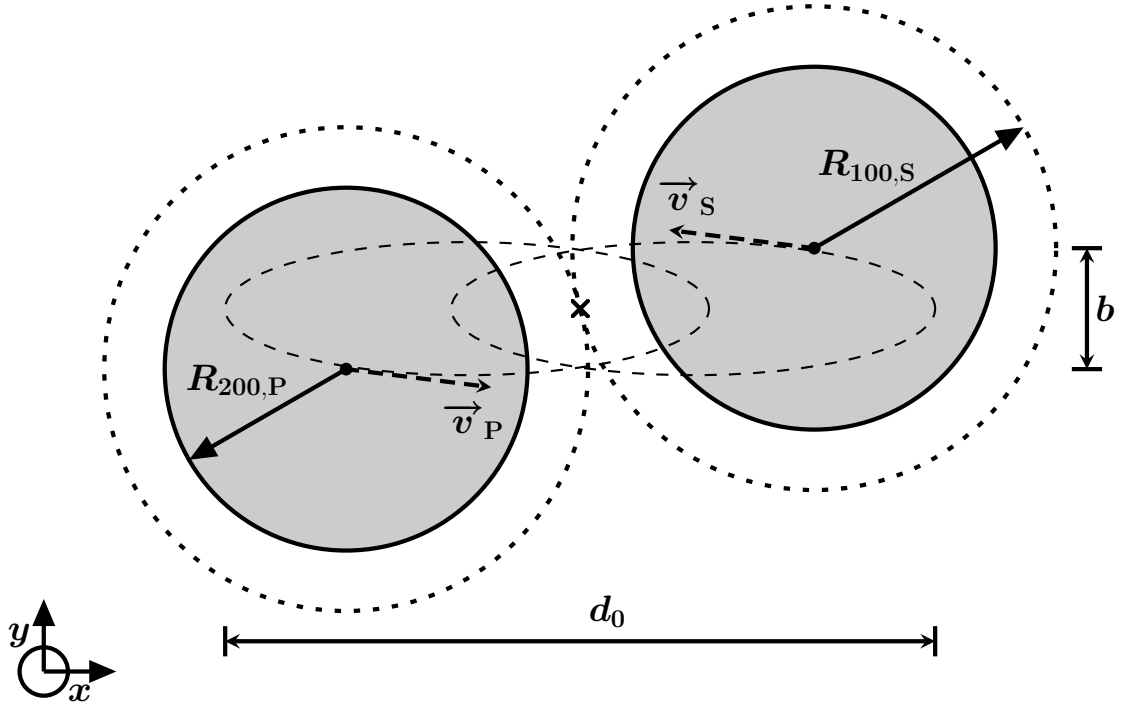


Fig. 4.— Initial geometric and kinematic configuration. The filled areas represent the virial ($R_{200}$) regions of the two clusters, while the "X" marks the center-of-mass. At the beginning of the simulations, the clusters are at a distance equal to the sum of their $R_{100}$ radii, while their centers are offset along the y-axis by the impact parameter, $b$. The mergers are initialized on elliptical paths with velocities consistent with their orbital angular momenta, set by their kinematics at the turnaround radius, $d_0$.

velocities. We begin by following the argument of Sarazin (2002) that the orbital angular momentum, $J_{\rm orb}$, is the difference between the initial and final momenta of the merging clusters. This leads to an initial transverse velocity,

$$v_0 = \lambda \sqrt{\frac{G(M_P + M_S)}{d_0}}\, f(M_P, M_S)\,, \tag{16}$$

where the function $f(M_P, M_S)$ accounts for the internal energies and angular momenta of the clusters,

$$f(M_P, M_S) = \frac{(M_P + M_S)^3}{M_P^{3/2} M_S^{3/2}} \left[1 - \frac{M_P^{5/3} + M_S^{5/3}}{(M_P + M_S)^{5/3}}\right]^{3/2} . \tag{17}$$

With knowledge of the initial distance and velocity, the Keplerian orbit is fully determined. The eccentricity is given by

$$e = \sqrt{1 + \frac{2E_{\rm orb}\, J_{\rm orb}^2}{\mu\, (G\, M_P\, M_S)^2}}\,, \tag{18}$$

where $E_{\rm orb}$ is the orbital energy, and $\mu = (M_P\, M_S)/(M_P + M_S)$ is the reduced mass of the system (see Landau & Lifshitz 1969, §15).

At the initial position $(d, \phi)$ in our simulations, where $\phi$ is the true anomaly (i.e., the angle measured from the pericenter with respect to the center of mass), the velocity may be obtained by conserving energy, and it is given by

$$v = \sqrt{v_0^2 + \frac{2G(M_P + M_S)}{d} \left(1 - \frac{d}{d_0}\right)}\,. \tag{19}$$

We need to determine the velocity components along the coordinate axes. To do this, we start with the Cartesian coordinates of an orbiting mass with respect to the center of mass (Landau & Lifshitz 1969, eqn. (15.11)), expressed in terms of the eccentric anomaly, $\xi$, (measured with respect to the center of the ellipse), that is,

$$x = \alpha(\cos\xi - e)\,;\; y = \alpha\sqrt{1 - e^2}\, \sin\xi\,, \tag{20}$$

where $\alpha$ is the semi-major axis. The two angles are related via

$$\cos\xi = \frac{e + \cos\phi}{1 + e\cos\phi} \tag{21}$$

$$\sin\xi = \frac{\sqrt{1 - e^2}\, \sin\phi}{1 + e\cos\phi}\,. \tag{22}$$

The Cartesian coordinates can be expressed in terms of the true anomaly as

$$x = \alpha\left(1-e^2\right)\,\frac{\cos\phi}{1+e\cos\phi} \tag{23}$$

$$y = \alpha\left(1-e^2\right)\,\frac{\sin\phi}{1+e\cos\phi}\,. \tag{24}$$

We differentiate with respect to time to obtain the velocity components, which are equal to

$$v_x = \alpha\left(1-e^2\right)\frac{\sin\phi}{(1+e\cos\phi)^2}\,\dot{\phi} \tag{25}$$

$$v_y = \alpha\sqrt{1-e^2}\frac{e+\cos\phi}{(1+e\cos\phi)^2}\,\dot{\phi}\,. \tag{26}$$

In terms of the total velocity, then, the velocity components are

$$\frac{v_x}{v} = -\sqrt{1-e^2}\frac{\sin\phi}{1+e\cos\phi} \tag{27}$$

$$\frac{v_y}{v} = \frac{e+\cos\phi}{1+e\cos\phi}\,. \tag{28}$$

These relations are useful because they simplify the relation for the angular momentum conservation. In fact, the angular momentum may now be written as

$$J_{\rm orb} = \mu dv\,\frac{\cos\phi\,(e+\cos\phi)+\sqrt{1-e^2}\,\sin^2\phi}{1+e\cos\phi}\,. \tag{29}$$

The only unknown in the equation is the true anomaly, $\phi$. In practice, we solve numerically for the root of the function

$$g(\phi) = \frac{d_0 v_0}{dv}\,(1+e\cos\phi) - \left(\cos\phi\,(e+\cos\phi)+\sqrt{1-e^2}\,\sin^2\phi\right)\,, \tag{30}$$

and fully determine the dynamics of the relative motion. The velocities of the individual clusters are assigned according to their masses.

### *3.3.1. Comparison to Cosmological Simulations*

We compare the orbital properties of our mergers to published work on the distribution of halo infall velocities. As is customary, we compute the relative velocity at the time the subcluster crosses the virial radius of the primary cluster (here taken at $\Delta = 100$, as in Vitvitska et al. 2002), and express it in units of the circular velocity at that radius. We find that for the ensemble of our simulations, the relative velocity is $v_{\rm rel} \approx (1.01 \pm$

$0.06)\,V_c(R_{\rm vir})$ in good agreement with the results of Vitvitska et al. (2002) and Tormen (1997), $v_{\rm rel}/V_c \approx 1.1 \pm 0.1$. We also compute the statistics of the radial and tangential velocity components. We do not include the head-on mergers in these calculations and we investigate the properties of major mergers (with mass ratios $M_P/M_S < 3$) and minor mergers ($M_P/M_S > 3$) independently to allow a direct comparison to the results of Vitvitska et al. (2002). Major mergers have radial velocities $v_{\rm rad}/V_c \approx 1.099 \pm 0.034$ and tangential velocities $v_{\rm tan}/V_c \approx 0.145 \pm 0.060$. Similarly, minor mergers have radial and tangential velocities of $v_{\rm rad}/V_c \approx 1.029 \pm 0.012$ and $v_{\rm tan}/V_c \approx 0.146 \pm 0.058$, respectively. The radial velocities of major mergers are slightly lower than expected, but consistent with cosmological simulations nevertheless. The tangential velocities are largely independent of the mass ratio of the merging clusters, but vary only with the angular momentum of the collision. In fact, we have determined that the tangential velocity is roughly $0.073\,V_c$ for $\lambda = 0.025$, $0.145\,V_c$ for $\lambda = 0.050$, and $0.217\,V_c$ for $\lambda = 0.075$, following a linear trend with the orbital spin (of slope $\approx 2.88$). Our tangential velocities are low compared to the dispersion measured by Vitvitska et al. (2002), $\sigma_\perp/V_c \approx 0.4$–$0.6$. However, as pointed out by Poole et al. (2006), their values are probably inflated by systems that are experiencing second or third infalls, and which probably have more isotropic velocities. In addition, the values of $\lambda$ we have selected to study do not cover the entire range (0–0.15) measured by Vitvitska et al. (2002). Extrapolating our results to $\lambda = 0.15$ we obtain a tangential velocity of $0.433\,V_c$. We conclude that our simple dynamical model produces orbits that are consistent with the results of cosmological simulations for the range of angular momenta we explore.

### 3.4. Simulation Properties and Naming Scheme

Table 2 presents the basic properties of our mergers. Each model is identified by the sequence M*x:y:z*, where *x, y,* and *z* refer to the primary cluster mass, the subcluster mass and the value of $1000\lambda$ for the collision. Notice that, for a given $\lambda$, the impact parameter in units of the virial radius varies little across our mergers with values in the range $b = 0.13$–$0.17$ for $\lambda = 0.025$, $b = 0.26$–$0.34$ for $\lambda = 0.050$, and $b = 0.4$–$0.5$ for $\lambda = 0.075$. The side-length of the computational cube varies in the range 5–30 Mpc in our simulations. The number of particles used to model the subclusters varies with the cluster masses and their ratio, and specific numbers for all mergers are given in Table 3. Note that the number of subcluster gas particles is determined by the mass ratio alone (see equation 3), while the number of subcluster DM particles depends slightly on the gas fraction values of the two clusters as well. The corresponding mass resolution, which depends on the primary cluster mass, covers two orders of magnitude and is presented in Table 4. We discuss the convergence properties of our simulations in § 5.

In the following, unless a specific merger-ID is given, we shall refer to collisions by means of the primary cluster mass, which we call a *simulation* or *merger suite*, and rely on the context to distinguish the specific collision. For instance, the merger M200:020:75 will be referred to as the "M200 merger" when we discuss maximum offset unequal-mass mergers.

Table 2. List of Merging Clusters Simulations[†]

| Merger ID | $b$[a] ($R_{200}$) | $b_{\rm phys}$ (Mpc) | $L_{\rm box}$[b] (Mpc) |
|---|---|---|---|
| (1) | (2) | (3) | (4) |
| M200.0:200.0:0 | 0 | 0 | 29.351 |
| M200.0:200.0:25 | 0.17 | 0.443 | 29.317 |
| M200.0:200.0:50 | 0.338 | 0.877 | 29.219 |
| M200.0:200.0:75 | 0.5 | 1.299 | 29.06 |
| M200.0:100.0:0 | 0 | 0 | 26.308 |
| M200.0:100.0:25 | 0.154 | 0.401 | 26.277 |
| M200.0:100.0:50 | 0.306 | 0.795 | 26.187 |
| M200.0:100.0:75 | 0.453 | 1.178 | 26.041 |
| M200.0:040.0:0 | 0 | 0 | 23.231 |
| M200.0:040.0:25 | 0.141 | 0.367 | 23.202 |

[†]Table 2 is published in its entirety in the electronic edition of ApJ. A portion is shown here for guidance regarding its form and content.

[a]Impact parameter in units of the primary cluster's virial radius.

[b]Side length of simulation cube.

Table 3. Numbers of Subcluster Particles

| Merger ID (1) | $N_{\rm DM,S}$ (2) | $N_{\rm ICM,S}$ (3) |
|---|---|---|
| M200.0:100.0:0 | 252835 | 234230 |
| M200.0:040.0:0 | 102524 | 85960 |
| M200.0:020.0:0 | 51749 | 40268 |
| M100.0:050.0:0 | 252626 | 234230 |
| M100.0:020.0:0 | 102338 | 85960 |
| M100.0:010.0:0 | 51620 | 40268 |
| M080.0:040.0:0 | 252563 | 234230 |
| M080.0:016.0:0 | 102282 | 85960 |
| M080.0:008.0:0 | 51581 | 40268 |
| M060.0:030.0:0 | 252484 | 234230 |
| M060.0:012.0:0 | 102211 | 85960 |
| M060.0:006.0:0 | 51532 | 40268 |
| M040.0:020.0:0 | 252377 | 234230 |
| M040.0:008.0:0 | 102116 | 85960 |
| M040.0:004.0:0 | 51467 | 40268 |
| M020.0:010.0:0 | 252206 | 234230 |
| M020.0:004.0:0 | 101964 | 85960 |
| M020.0:002.0:0 | 51361 | 40268 |
| M010.0:005.0:0 | 252049 | 234230 |
| M010.0:002.0:0 | 101824 | 85960 |
| M010.0:001.0:0 | 51264 | 40268 |
| M008.0:004.0:0 | 252001 | 234230 |
| M008.0:001.6:0 | 101781 | 85960 |
| M006.0:003.0:0 | 251941 | 234230 |
| M006.0:001.2:0 | 101728 | 85960 |
| M004.0:002.0:0 | 251860 | 234230 |
| M002.0:001.0:0 | 251729 | 234230 |

Table 4. Mass Resolution

| $M_{200,\mathrm{P}}$ ($10^{13}\,M_\odot$) (1) | $\Delta M_{\mathrm{DM}}$ ($10^{7}\,M_\odot$) (2) | $\Delta M_{\mathrm{ICM}}$ ($10^{6}\,M_\odot$) (3) |
|---|---|---|
| 200 | 339.04 | 609.6 |
| 100 | 171.44 | 285.6 |
| 80 | 137.624 | 223.76 |
| 60 | 103.668 | 163.32 |
| 40 | 69.52 | 104.8 |
| 20 | 35.09 | 49.1 |
| 10 | 17.7 | 23 |
| 8 | 14.198 | 18.016 |
| 6 | 10.684 | 13.152 |
| 4 | 7.156 | 8.44 |
| 2 | 3.604 | 3.954 |
| 1 | 1.814 | 1.852 |

### 3.5. Simulation Code and Numerical Setup

We have used the TreeSPH code Gadget-2 (Springel 2005) for our simulations. Gadget-2 is a Lagrangian code that uses tracer particles to follow the dynamics of the dark matter and gas. The gas is evolved with the Smooth Particle Hydrodynamics method (SPH; see Springel 2010, for an excellent review). In SPH the fluid is modeled with discrete particles, and continuous properties are obtained by interpolating over a predefined number, $N_{\rm sph}$, of nearest neighbors. We have used $N_{\rm sph} = 64$ in all our calculations. We experimented with various values in the range 32–512 and arrived at the value of choice because it offers a decent reconstruction of the initial clusters' density profiles (the reproduced profile had a higher normalization by a factor of 1.25 and large errors) for a reasonable amount of execution time. Note that due to this overestimation of the density profile our initial clusters undergo some readjustment at the start of the simulations that lasts about 300–600 Myr; in all cases, however, our initial cool cores are not erased by this process. Gravitational forces are obtained with the Tree method, a fast, $\mathcal{O}(N \log_2 N)$, algorithm that employs a hierarchical partition of space to facilitate efficient force calculations. Nearby particles are accounted for by direct summation, while more distant particles are grouped together in a single multipole force. We experimented with the particle-mesh algorithm for the computation of long-range forces, but found that the Tree algorithm resulted in final remnants whose structure was in slightly better agreement with the expected clusters.

We have employed periodic boundary conditions in Newtonian space ($\Omega_\Lambda = 0$), making sure that the merger takes place at the center of the simulation volume. In fact, we have chosen the central cube of the domain to be slightly larger than the span of the merging clusters along the x-axis, so that most of the $R_{100}$ cluster regions are within the central $(L/2)^3$ volume. The domain size for our mergers is listed in Table 2. This makes certain that the Ewald forces on the clusters from all the periodic images of the merger are negligible. Note that the total mass beyond the central simulation volume amounts to no more than $\sim 20\%$ of the virial mass of the system.

The last ingredient we need to determine is the gravitational softening. We have explored the method of Dehnen (2001), which yields an "optimal" softening length between forces dominated by shot-noise (two-body interactions) for small softening lengths, and forces biased by too large softening values. We have compared this method to using a fixed fraction of the virial radius of the primary cluster for the softening, and we did not find that the exact value of the softening scale significantly affected our results, although the fixed-length runs tended to execute faster. In our calculations, we have used softening lengths that amount to 0.5% of $R_{200}$.

The computations were carried out on TeraGrid facilities and required $\sim$ 40,000 comput-

ing hours on Lonestar and Ranger at the Texas Advanced Computing Center, Abe and Cobalt at the National Center for Supercomputing Applications, and QueenBee at the Louisiana Optical Network Initiative. A small number of simulations (8) was also completed on the 384-core Hyades Beowulf cluster owned by the Astronomy Department at the University of Virginia.

## 4. Cluster Detection

For the purposes of our analysis it is important to isolate the cluster virial regions from the external gas and dark matter in which they are embedded. We use *AMIGA's Halo Finder* (AHF, Knollmann & Knebe 2009; Gill et al. 2004), version 1.0 for that purpose.

AHF is an adaptive mesh refinement code that can be used to extract halos from cosmological numerical simulations. It operates by interpolating the density field of a simulation box on a user-specified grid and by recursively refining it until a minimum number of particles per cell is met. On the basis of this grid hierarchy, AHF constructs a density tree which is then used to detect halos and their substructure, if any. Note that in the computation of virial masses, dynamical information is taken into account as well, and any unbound particles are removed.

We have slightly modified the code for ease of use with our data, and to report structural parameters at four different overdensity levels. For cluster detection, we require a minimum overdensity of 190 times the critical density at $z = 0$, ignore particles with velocities greater than 1.5 times the local escape velocity, and ignore halos that contain fewer than 10,000 particles, that is less than 1 percent of the initial primary cluster mass. We have experimented with various cut-offs and found that halos with fewer particles are typically very overdense ($\Delta > 2500$). For the adopted cutoff, we are able to detect halos until after the second core-crossing.

Utilizing the information provided by AHF, we are able to produce aggregate (e.g. X-ray observables), and differential (e.g., spherical profiles) measures for the primary cluster at overdensities $\Delta = 200$ and 500 relative the critical density. All quantities discussed below and in the following papers, unless otherwise specified, are computed in this manner. In addition, unless noted to the contrary, we track the particles of both clusters jointly after the subcluster crosses the virial radius of the primary cluster.

## 5. Convergence of Simulations

As Table 4 illustrates, our simulation set employs a varying mass resolution that depends on the mass of the primary cluster. Ideally, the mass resolution should be the same across the set, as concerns may arise over how best to compare the results of various calculations. If we were to adopt a common mass resolution, and chose to downgrade the resolution of $10^{13}\ M_\odot$ clusters by an order of magnitude, the amount of simulation data would increase by a factor of 5 (about 2 billion particles). In addition, it is often the case that adiabatic SPH simulations converge for a number of particles, so that improving the resolution would not yield significantly more accurate results. By contrast, in physics-rich simulations the development of fluctuations may depend sensitively on the adopted resolution. In light of these considerations, we have opted to use a fixed number of particles per primary halo, with the understanding that the simulation results have converged.

To this end, we have conducted a convergence study of one of our mergers with particle numbers in the range $2\times10^5$–$10^7$. This is a range of two orders of magnitude about the adopted resolution. The merger we have used for this test is M010.0:001.0:75, that is, a maximum offset 10:1 merger between a $10^{14}M_\odot$ and a $10^{13}\,M_\odot$ cluster. We selected this merger, because it is the lowest primary mass collision with a mass ratio of 10, and it possesses the lowest gas fractions in our sample. The most oblique collision of that suite should then be the most sensitive to the effects of the varying mass resolution.

In our high resolution resimulation of this collision, we use the mass resolution that corresponds to the $10^{13}\,M_\odot$ suite (see Table 4, bottom line). Figure 5 illustrates the comparison between the high resolution and production runs. The X-ray luminosity integrated within $R_{500}$ (Fig. 5, *top left* panel) gauges the evolution of the gas density profiles and their near coincidence at all times suggests that there is little dependence on the particle mass. Likewise, the integrated Sunyaev-Zel'dovich effect measures the total thermal energy content (Fig. 5, *top right* panel), observed along the z-axis within the projected $R_{500}$, indicates that the pressure is mostly converged as well. Taken together, these results suggest that the temperature does not depend significantly on the resolution. We have confirmed that this is indeed the case by inspecting the time variation of the mass-weighted temperature ($T_{\rm mg}$; not shown).

It is also important to investigate the convergence of forces in our simulation. To achieve that, we employ the virial disequilibrium parameter (Ricker 1998; Ricker & Sarazin 2001; Poole et al. 2006), for the dark matter and the ICM within $R_{500}$. The two parameters are defined by

$$V_{\rm DM} \;=\; 1+\frac{2T_{\rm DM}}{W_{\rm DM}+S_{\rm DM}} \tag{31}$$

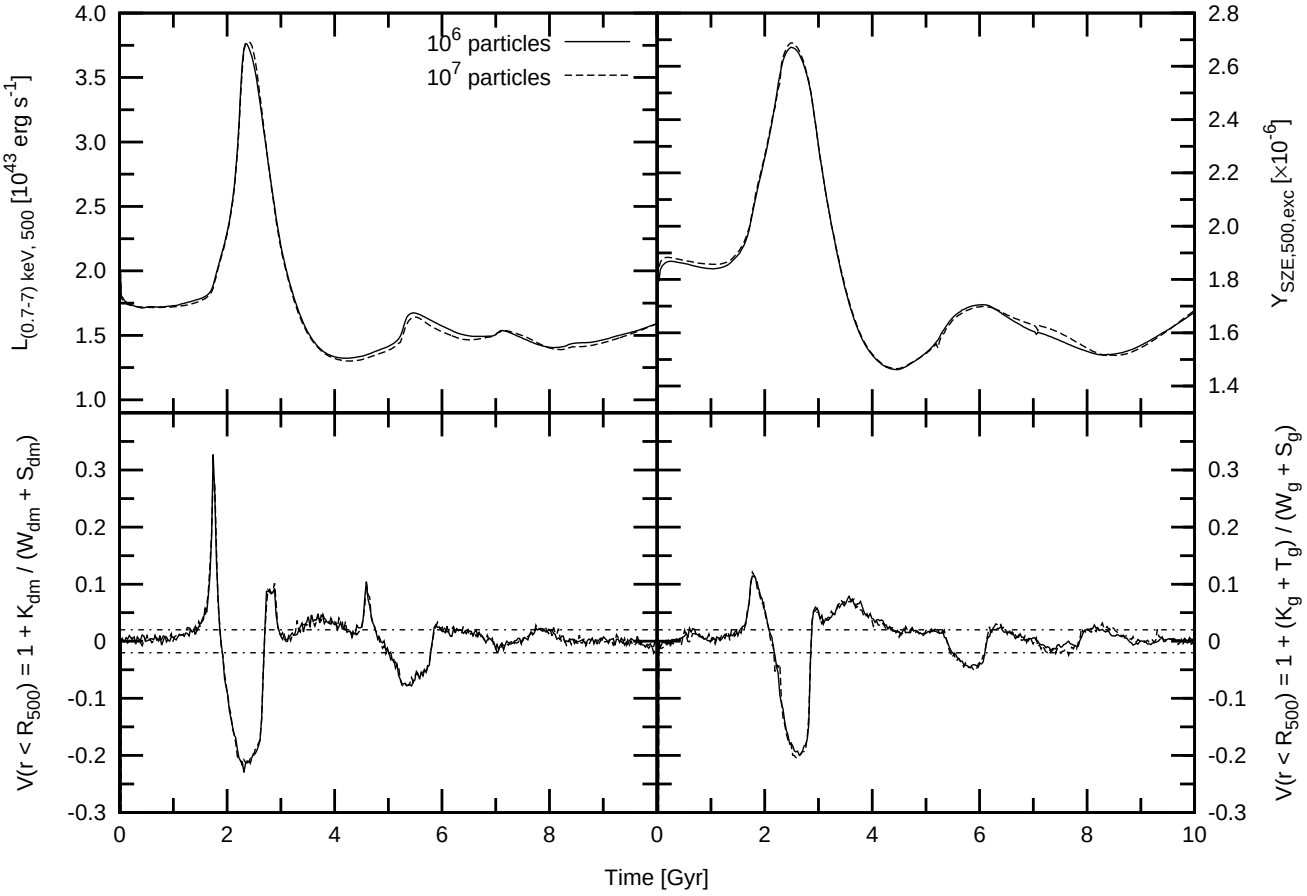


Fig. 5.— Time evolution of primary cluster properties for runs with 1 million (red solid line) and 10 million (green dashed line). *(Top Left)* X-ray luminosity in the (0.7–7) keV band integrated within the central $R_{500}$. *(Top Right)* Total thermal energy content within the projected $R_{500}$ as viewed along the z-axis. *(Bottom)* Instantaneous virial disequilibrium parameters for the dark matter *(Left)* and the gas *(Right)*. The horizontal lines represent the typical 2 percent errors (see text). All parameters are within 2 percent of their higher resolution counterparts, almost at all times.

$$V_{\rm ICM} \;=\; 1 + \frac{2(T_{\rm ICM} + U_{\rm ICM})}{W_{\rm ICM} + S_{\rm ICM}}\,, \tag{32}$$

where $T$ refers to the total kinetic energy within the integration volume, and $U_{\rm gas}$ is the total thermal energy of the ICM. The virial of Clausius, $W$, is defined as

$$W = \sum_i \sum_j \boldsymbol{F}_{ij} \cdot \boldsymbol{r}_{ij}\,, \tag{33}$$

where the sum over $i$ extends over all the particles within the volume of interest and the sum over $j$ extends over all the particles in the simulation. Here, $\boldsymbol{F}_{ij}$ is the force of particle $j$ on particle $i$, and $\boldsymbol{r}_{ij}$ is the separation of the two particles. The virial of Clausius would reduce to twice the potential energy of the $R_{500}$ volume if all particles beyond that region could be ignored.

The $S_{\rm DM}$ and $S_{\rm gas}$ terms correspond to the surface integrals of the kinetic and thermal energy that arise due to the finite extent of the integration volume. They are defined as

$$S_{\rm DM} \;=\; \int dA\, \rho_{\rm DM}\, \overline{v_r^2}\, r\,, \tag{34}$$

$$S_{\rm ICM} \;=\; \int dA\, (P + \rho_{\rm ICM}\, \overline{v_r^2})\, r\,, \tag{35}$$

where the integral extends over the surface that bounds the volume. In our calculations, we approximate these integrals by computing volume integrals over a spherical shell of width $\Delta r$ that contains $N$ particles, that is,

$$S_{\rm DM} \;\approx\; \frac{1}{\Delta r} \sum_i m_{\rm DM,i}\, v_{\rm r,i}^2\, r_i\,, \tag{36}$$

$$S_{\rm ICM} \;\approx\; \frac{1}{\Delta r} \sum_i m_{\rm ICM,i}\, (\frac{P_i}{\rho_i} + v_{\rm r,i}^2)\, r_i\,. \tag{37}$$

A brief derivation of these equations is presented in Appendix C. We take $N = 5000$ in our calculations. Note that since the other terms involve all particles within the volume of interest, the error in the disequilibrium parameter is driven by the surface terms. In our case, this is roughly $1/\sqrt{N} \approx 1.4\%$. However, we take our error to be 0.02, consistently with previous work; this also determines the critical value below which our mergers may be considered as relaxed, i.e., $|V| \leq 0.02$.

The rigorous definition of the Virial Theorem requires taking averages of equations (31) and (32) over sufficiently long timescales. In our present discussion, however, we consider instantaneous values of the disequilibrium parameters, because we are primarily interested in gauging differences between particle forces; these would be damped in harmonic averages.

As shown in the bottom panels of Figure 5, there is a close correspondence between the evolution of the disequilibrium parameters between the two runs. In fact, the effect of the lower resolution simulation is to introduce some scatter about the higher resolution curve, that is smaller than the uncertainty in the parameters.

We may then conclude that our simulations are converged for the adopted resolution.

## 6. Summary

In this paper, which is the first of a series of papers, we have presented a description of the numerical method employed in the construction of the 156 binary merger simulations that make up the *SLAM* database. The initial conditions are based on the results of semi-analytical models of cluster structure, which are in very good agreement with recent *Chandra* and *XMM-Newton* observations. The model clusters are in excellent agreement with scaling relations in the mass range $10^{13}$ $M_{\odot}$ – $10^{15}$ $M_{\odot}$.

Our simulations employ three free parameters; the mass of the primary cluster, the ratio of the primary cluster mass over the subcluster mass and the orbital spin of the collision. We have allowed the primary cluster mass to take 12 values in the range 1–200$\times 10^{13}$ $M_{\odot}$, the mass ratio to vary between 1 and 10, and we have used results from cosmological simulations to select 4 values for the dimensionless orbital spin. We have enforced a minimum mass for the subcluster of $10^{13}$ $M_{\odot}$. In total, 156 simulations are modeled.

The simulations are run with the SPH code Gadget-2 with a mass resolution that varies with the primary cluster mass. We have compared a selected prototype collision with a resimulation having a mass resolution refined by almost an order of magnitude. We have verified that the mass resolution differences are smaller than the statistical error of the measured quantities and that the simulations are converged for the adopted resolution.

The following papers of this series address the self-similarity of merging events, the observational signatures of mergers and their effects on scaling relations as a function of the system mass, hydrostatic mass biases during the course of mergers for X-ray and SZE observations, and the implications of our findings for cosmological surveys.

MC would like to thank A.J.R. Sanderson for making himself available to clarify certain aspects of a recent paper, and Amalia Hicks and Ming Sun for useful discussions. Support for this work was provided by the National Aeronautics and Space Administration through Chandra awards TM7-8010X, GO9-0135X, GO9-0148X, GO1-12159A, GO1-12169X, issued by the Chandra X-ray Observatory Center, which is operated by the Smithsonian Astrophys-

ical Observatory for and on behalf of the National Aeronautics Space Administration under contract NAS8-03060, through NASA Suzaku grants NNX09AH25G and NNX09AH74G and by the NASA ADAP grant NNX11AD15G. This research was supported in part by the National Science Foundation through TeraGrid resources provided by the Texas Advanced Computing Center, the Louisiana Optical Network Initiative and the National Center for Supercomputing Applications under grant numbers TG-AST080001N and TG-AST090040. BWO acknowledges support by NASA ATFP grant #08-ATFP08-0028, NSF AST grant #0908819, and Michigan State University's Institute for Cyber-Enabled Research.

## A. Input Model Entropy Profiles

We present a detailed comparison of the entropy profiles of our initial models to the observations of Sun et al. (2009). We reproduce their Figures 12 and 15 for the 20 clusters used as initial conditions in our simulations and compare our results to their best-fit relations. When possible, we opt to compare to results based on the Tier 1 clusters, i.e., groups observed out to $R_{500}$ or beyond. In our calculations, we use spectroscopic-like temperatures, $\mathrm{T}_X$, following the weighting procedure of Vikhlinin (2006, mixT, see footnote 1), and integrating our models along a cylindrical annulus $(0.15–1)\times R_{500}$. We refer to this temperature as $T_{500}$.

The entropy profiles of our groups are in good agreement with the measurements within $R_{1000}$. Figure 6 displays a comparison to the S09 best-fit relations, and illustrates that our clusters are consistent with the joint fits to the S09 cluster and group data. Small discrepancies exist around $R_{500}$, but only for $T_{500} < 2\,\mathrm{keV}$. Figure 1 indicates that the groups in our sample are somewhat underdense compared to the observations of S09 for $M_{500} \lesssim 10^{14}\,M_\odot$ ($T_{500} \lesssim 2\,\mathrm{keV}$). We have thus explored the entropy dependence on the virial gas fraction by increasing the normalization of equation (3) by 15%; this brings the lowest mass groups with $T_{500} \lesssim 0.8$ keV to near exact agreement with the $f_{\rm gas}(M)$ relation of S09. The entropy at $R_{500}$ becomes consistent with the observations at the expense of bigger offsets at lower cluster-centric radii. Massive clusters are not affected by this change noticeably. This suggests that, in principle, slightly larger values for the gas fraction may improve somewhat the correspondence of our models to observed entropy profiles, although this would render the $f_{\rm gas}$ distribution of more massive clusters inconsistent with the observations of V09.

We have also examined the effects of a steeper entropy slope for our groups by using a higher value, $\alpha_{13} = 0.7$, but the deviations at $R_{500}$ become more pronounced. Therefore, these differences are most likely due to the lower gas fraction in our models, or alternatively to the fact that the entropy slope varies with the group radius (see S09), while our models possess a constant value throughout the cluster volume. Nevertheless, the agreement of the entropy scale at $R_{500}$ does not significantly affect the global properties of our clusters and groups.

## B. Input Model Scaling Relations

The scaling properties of our input models are important in understanding the efficiency of rescaling, as well as the behavior of our mergers on the relevant scaling-relation planes (to be treated in a subsequent papers). As discussed in § 2, our calibration against the models of V06a produced models with properties very similar to observed scaling relations. Here we

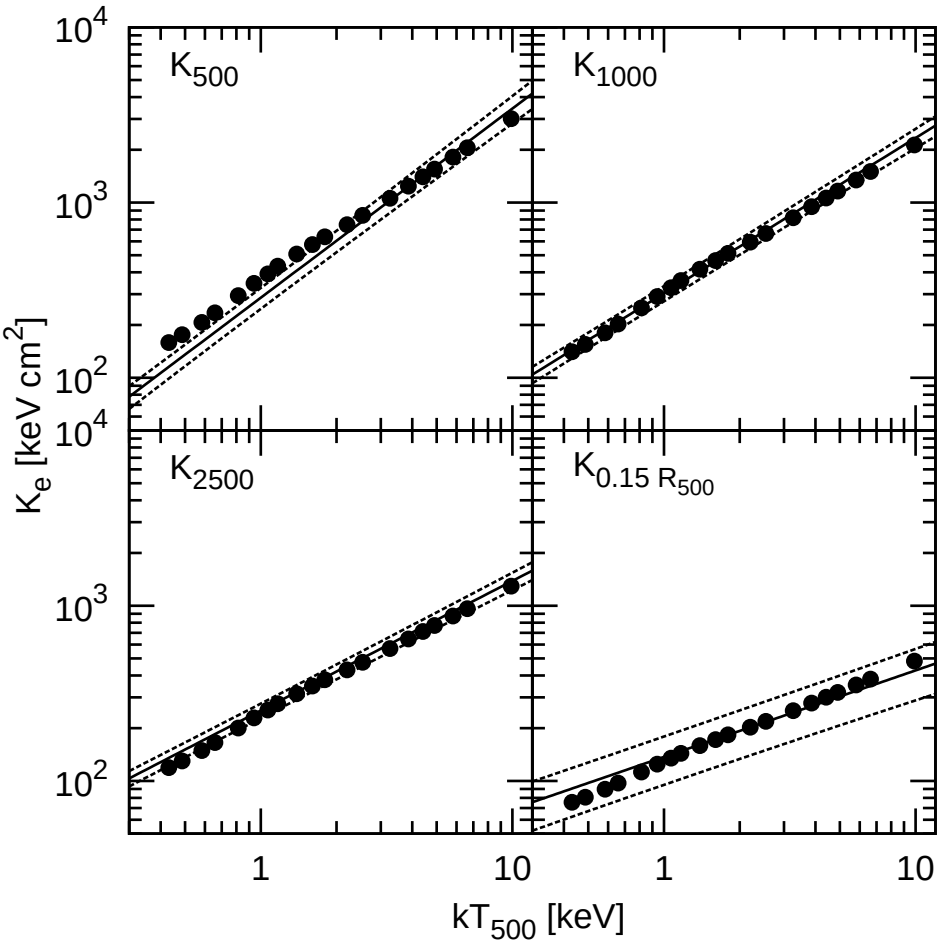


Fig. 6.— Entropy at four radii compared to the corresponding observational results from S09. Our models are in good agreement with the best-fit power-laws. Small deviations occur for cool clusters at $R_{500}$, which suggest a steepening of the profiles at the cluster outskirts. This is most likely due to the variation of the entropy slope with radius in real groups (see text).

present an extension of that comparison down to the scales relevant to our groups, shown in Figure 7.

Our clusters are in excellent agreement in with the $L_X$–$M_{200}$ and $L_X$-$T$ relations of Eckmiller et al. (2011). Although small deviations from the best-fit relations may be seen at both luminosity ends, suggesting our clusters are marginally overdense or cooler compared to the best-fit prediction, our results are fully consistent within the measured errors and intrinsic scatter of these relations. Our clusters are in excellent agreement with the $Y_{\rm SZE}$–$M_{500}$ and $M_{500}$–$T_{500}$ relations of Arnaud et al. (2010) and S09, respectively. Similar deviations at around 1–2 keV may be seen in the $M_{500}$–$T_{500}$ relation, suggesting slightly cooler halos than the scaling relation predicts. Finally, our initial clusters are also in excellent agreement with the $M_{2500}$–$y_0$ relation of Morandi et al. (2007), which gauges the line-of-sight pressure integral through the centers of our clusters. The relation is obtained from observations of bright X-ray clusters, that is, it has been verified over a rather restricted mass range. Our clusters are in excellent agreement with the relation over that mass range, and it also seems to be in excellent agreement with the extrapolation of this relation at lower masses.

Overall, our initial cluster models are in very good agreement with the above scaling relations, except for small deviations at the group scale.

## C. Derivation of Surface Terms

We present a brief derivation of the surface terms used with the virial disequilibrium parameters, based mainly on Binney & Tremaine (1987).

The derivation is almost identical to that presented in the book, except that, due to the finite extent of the integration volume, equation (4–73a) therein must include the surface term obtained from the application of the divergence theorem, that is,

$$\begin{aligned} \int\limits_V x_k \, \frac{\partial(\rho \overline{v_i \, v_j})}{\partial x_i} \, d^3x &= \int\limits_S x_k \, \rho \, \overline{v_i \, v_j} \, d^2\boldsymbol{S} - 2 \, K_{\rm jk} \\ &= \int\limits_S r \, \rho \, \overline{v_r^2} \, dA - 2 \, K_{\rm jk} \, . \end{aligned} \tag{C1}$$

In the second integral the only velocity components that survive are those normal to the bounding surface, while the third integral is equal to the trace of the tensor. From the definition of the density, eqn. (4–20), and equation (4–24b) therein, we have

$$\rho \, \overline{v_r^2} = \int d\rho \, v_r^2 \, , \tag{C2}$$

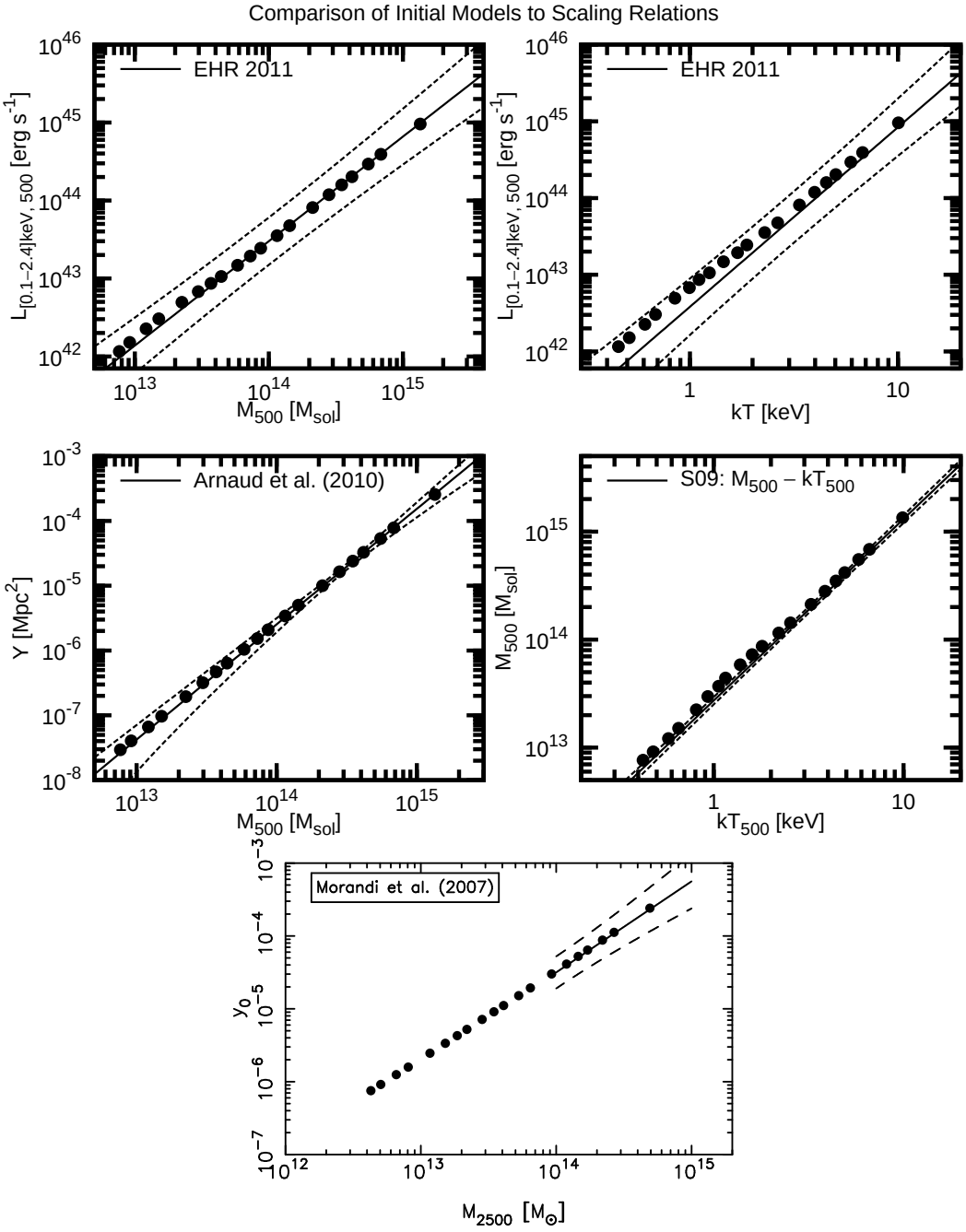


Fig. 7.— Comparison of our initial models to scaling relations. *(Top, Left)* $L_X$–$M_{200}$ relation of Eckmiller et al. (2011) in the ROSAT band (0.1–2.4 keV). *(Top, Right)* $L_X$–$T$ relation of Eckmiller et al. (2011). *(Middle, Left)* $Y_{\rm SZE}$–$M_{500}$ relation of Arnaud et al. (2010). *(Middle, Right)* $M_{500}$–$T_{500}$ correlation for our input clusters and groups, compared against the best-fit relation of S09 to their combined sample of groups and clusters. *(Bottom)* $M_{2500}$–$y_0$ relation compared against the best-fit relation of Morandi et al. (2007) for cool-core cluster masses ($M_{2500}$) in the range $10^{14}$–$10^{15}\,M_\odot$.

so the integral of equation (C1) becomes

$$\begin{aligned}
\int_S r\,\rho\,\overline{v_r^2}\,dA &= \frac{1}{\Delta r}\int_V r\,\rho\,\overline{v_r^2}\,dV \\
&= \frac{1}{\Delta r}\int_V dV \int d\rho\, r\, v_r^2 \\
&\approx \frac{1}{\Delta r}\int_V dV \sum_i \rho_i\, r_i\, v_{r,i}^2 \\
&\approx \frac{1}{\Delta r}\sum_i m_i\, r_i\, v_{r,i}^2\,. \qquad \text{(C3)}
\end{aligned}$$

These general conclusions apply for both the dark matter and the gas.

The disequilibrium parameter for the gas may also be obtained from Euler's equation of fluid dynamics. Here we focus on the term $-\boldsymbol{\nabla} P$, which we multiply by $r$ and integrate over volume to get

$$\begin{aligned}
-\int_V r\,\boldsymbol{\nabla} P\,dV &= -\int_S r\,P\,dA + \int_V (P\cdot\boldsymbol{\nabla}) r\,dV \\
&= -\int_S r\,P\,dA + 3\,(\gamma-1)\int_V \rho\,u\,dV\,, \qquad \text{(C4)}
\end{aligned}$$

where the first term corresponds to the pressure surface term and the second to the total thermal energy within the volume ($U_{\rm ICM}$ in equation 32), with $u$ representing the specific heat of the gas.

## REFERENCES

Anders, E., & Grevesse, N. 1989, Geochim. Cosmochim. Acta, 53, 197

Arnaud, M., Pointecouteau, E., & Pratt, G. W. 2007, A&A, 474, L37

Arnaud, M., Pratt, G. W., Piffaretti, R., Böhringer, H., Croston, J. H., & Pointecouteau, E. 2010, A&A, 517, A92

Binney, J., & Tremaine, S. 1987, Galactic Dynamics (Princeton University Press)

Brunetti, G., & Lazarian, A. 2011, MNRAS, 410, 127

Bullock, J. S., Dekel, A., Kolatt, T. S., Kravtsov, A. V., Klypin, A. A., Porciani, C., & Primack, J. R. 2001, ApJ, 555, 240

Buote, D. A., Gastaldello, F., Humphrey, P. J., Zappacosta, L., Bullock, J. S., Brighenti, F., & Mathews, W. G. 2007, ApJ, 664, 123

Dehnen, W. 2001, MNRAS, 324, 273

Donahue, M., Horner, D. J., Cavagnolo, K. W., & Voit, G. M. 2006, ApJ, 643, 730

Eckmiller, H. J., Hudson, D. S., & Reiprich, T. H. 2011, A&A, 535, A105

Edge, A. C., & Stewart, G. C. 1991, MNRAS, 252, 414

Faltenbacher, A., Allgood, B., Gottlöber, S., Yepes, G., & Hoffman, Y. 2005, MNRAS, 362, 1099

Ferrari, C., Govoni, F., Schindler, S., Bykov, A. M., & Rephaeli, Y. 2008, Space Sci. Rev., 134, 93

Finoguenov, A., Ponman, T. J., Osmond, J. P. F., & Zimer, M. 2007, MNRAS, 374, 737

Gill, S. P. D., Knebe, A., & Gibson, B. K. 2004, MNRAS, 351, 399

Gottlöber, S., & Yepes, G. 2007, ApJ, 664, 117

Hu, W., & Kravtsov, A. V. 2003, ApJ, 584, 702

Kaiser, N. 1986, MNRAS, 222, 323

Kazantzidis, S., Magorrian, J., & Moore, B. 2004, ApJ, 601, 37

Knollmann, S. R., & Knebe, A. 2009, ApJS, 182, 608

Komatsu, E., et al. 2009, ApJS, 180, 330

Kravtsov, A. V., Vikhlinin, A., & Nagai, D. 2006, ApJ, 650, 128

Kuijken, K., & Dubinski, J. 1994, MNRAS, 269, 13

Landau, L. D., & Lifshitz, E. M. 1969, Mechanics, ed. Landau, L. D. & Lifshitz, E. M.

Maughan, B. J. 2007, ApJ, 668, 772

Mitchell, N. L., McCarthy, I. G., Bower, R. G., Theuns, T., & Crain, R. A. 2009, MNRAS, 395, 180

Morandi, A., & Ettori, S. 2007, MNRAS, 380, 1521

Morandi, A., Ettori, S., & Moscardini, L. 2007, MNRAS, 379, 518 (MEM07)

Navarro, J. F., Frenk, C. S., & White, S. D. M. 1997, ApJ, 490, 493

Osmond, J. P. F., & Ponman, T. J. 2004, MNRAS, 350, 1511

Pearce, F. R., Thomas, P. A., & Couchman, H. M. P. 1994, MNRAS, 268, 953

Piffaretti, R., Jetzer, P., Kaastra, J. S., & Tamura, T. 2005, A&A, 433, 101

Ponman, T. J., Sanderson, A. J. R., & Finoguenov, A. 2003, MNRAS, 343, 331

Poole, G. B., Babul, A., McCarthy, I. G., Sanderson, A. J. R., & Fardal, M. A. 2008, MNRAS, 391, 1163

Poole, G. B., Fardal, M. A., Babul, A., McCarthy, I. G., Quinn, T., & Wadsley, J. 2006, MNRAS, 373, 881 (P06)

Popesso, P., Biviano, A., Böhringer, H., Romaniello, M., & Voges, W. 2005, A&A, 433, 431

Pratt, G. W., Croston, J. H., Arnaud, M., & Böhringer, H. 2009, A&A, 498, 361

Pratt, G. W., et al. 2010, A&A, 511, A85

Press, W. H., Teukolsky, S. A., Vetterling, W. T., & Flannery, B. P. 1992, Numerical recipes in C. The art of scientific computing, 2nd edn. (Cambridge University Press)

Randall, S. W., Sarazin, C. L., & Ricker, P. M. 2002, ApJ, 577, 579

Ricker, P. M. 1998, ApJ, 496, 670

Ricker, P. M., & Sarazin, C. L. 2001, ApJ, 561, 621 (RS01)

Ritchie, B. W., & Thomas, P. A. 2002, MNRAS, 329, 675

Roettiger, K., Burns, J. O., & Loken, C. 1996, ApJ, 473, 651

Roettiger, K., Loken, C., & Burns, J. O. 1997, ApJS, 109, 307 (R97)

Ruszkowski, M., & Oh, S. P. 2010, ApJ, 713, 1332

Sanderson, A. J. R., Ponman, T. J., Finoguenov, A., Lloyd-Davies, E. J., & Markevitch, M. 2003, MNRAS, 340, 989

Sarazin, C. L. 2002, in Astrophysics and Space Science Library, Vol. 272, Merging Processes in Galaxy Clusters, ed. L. Feretti, I. M. Gioia, & G. Giovannini, 1

Skillman, S. W., Hallman, E. J., O'Shea, B. W., Burns, J. O., Smith, B. D., & Turk, M. J. 2011, ApJ, 735, 96

Springel, V. 2005, MNRAS, 364, 1105

—. 2010, ARA&A, 48, 391

Springel, V., et al. 2005, Nature, 435, 629

Sun, M., Voit, G. M., Donahue, M., Jones, C., Forman, W., & Vikhlinin, A. 2009, ApJ, 693, 1142 (S09)

Takizawa, M. 1999, ApJ, 520, 514

Tormen, G. 1997, MNRAS, 290, 411

Vikhlinin, A. 2006, ApJ, 640, 710

Vikhlinin, A., Kravtsov, A., Forman, W., Jones, C., Markevitch, M., Murray, S. S., & Van Speybroeck, L. 2006, ApJ, 640, 691 (V06a)

Vikhlinin, A., et al. 2009, ApJ, 692, 1033

Vitvitska, M., Klypin, A. A., Kravtsov, A. V., Wechsler, R. H., Primack, J. R., & Bullock, J. S. 2002, ApJ, 581, 799

Wik, D. R., Sarazin, C. L., Ricker, P. M., & Randall, S. W. 2008, ApJ, 680, 17

ZuHone, J. A. 2011, ApJ, 728, 54 (Z11)